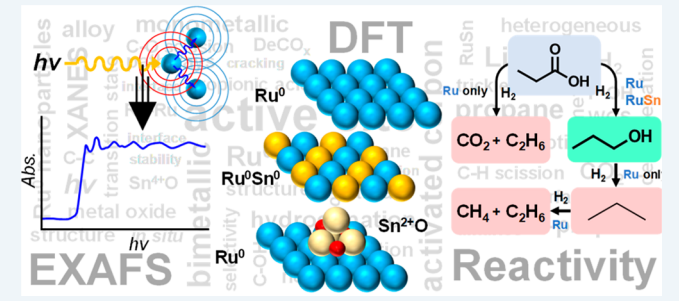


Inverse Bimetallic RuSn Catalyst for Selective Carboxylic Acid Reduction

Vassili Vorotnikov, † Todd R. Eaton, † Amy E. Settle, † Kellene Orton, † Evan C. Wegener, † Ce Yang, § Jeffrey T. Miller, † Gregg T. Beckham, * † † and Derek R. Vardon * † †

Supporting Information

ABSTRACT: Inverse bimetallic catalysts (IBCs), synthesized by sequential deposition of noble and oxophilic metals, offer potential reactivity enhancements to various reactions, including the reduction of carboxylic acids for renewable fuels and chemicals. Here, we demonstrate that an IBC comprising RuSn exhibits high selectivity for propionic acid reduction to 1-propanol, while Ru alone results in cracking. On RuSn, X-ray absorption spectroscopy identified Ru⁰ nanoparticles with a near-surface bimetallic Ru⁰Sn⁰ alloy and small SnO_x domains. Corresponding model surfaces were examined with density functional theory to elucidate the



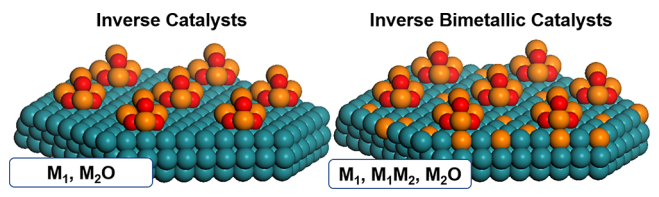
observed selectivity difference. Only selective hydrogenation is predicted to be favorable on SnO_x/Ru, with the SnO_x clusters facilitating C-OH scission and Ru enabling hydrogen activation. Intrinsic barriers along nonselective pathways suggest that the RuSn alloy and SnO_x resist cracking. SnO_x/Ru hydrogenation activity was supported experimentally by inhibiting hydrogenation with phenylphosphonic acid, differentiating the system from fully alloyed RuSn metallic nanoparticles. Overall, this work demonstrates a plausible mechanism for selective reduction of carboxylic acids and proposes a roadmap for rational design of IBCs.

KEYWORDS: propionic acid, 1-propanol, selective hydrogenation, aqueous-phase catalysis, ruthenium, ruthenium—tin alloy, tin oxide

■ INTRODUCTION

Understanding the structure and performance-enhancing mechanism of industrially relevant bimetallic catalysts remains a critical challenge for rational catalyst design, especially in the context of emerging renewable processes. 1,2 Aqueous-phase reduction of biologically derived carboxylic acids is one such transformation^{1,3-7} capable of producing alcohols that are suitable as fuel additives, 8,9 precursors to acrylonitrile, 10,11 or polymer precursors with potential for lower overall greenhouse gas emissions. 1,8,12-15 Typical catalyst candidates for selective reduction of carboxylic acids involve combinations of noble (e.g., Pd, Pt, or Ru) and oxophilic (e.g., Re, Ti, or Sn) metals, 1,16-25 but the precise nature of their sites remains unresolved.²⁶ Some investigations attributed unique reactivity to the synergy of metal and metal oxide functionalities, 2,16,18,20,21,27-37 analogous to CO₂ hydrogenation observed over inverse catalysts, with inverse catalyst defined as the sequential deposition of metal oxide on top of a noble metal, or metal-supported metal oxides (Scheme 1, left).^{38–40} Other studies point to bimetallic alloys being responsible for catalyst enhancement. 17,22-24,41,42 The possibility of alloying distinguishes inverse bimetallic catalysts (IBCs) from inverse catalysts and complicates the ability to interpret the active sites

Scheme 1. Representations of Inverse-Prepared Catalysts a,b



^aHere inverse is defined as a metal oxide sequentially deposited on top of a noble metal. ^bIn this figure, M₁ represents Ru, and M₂O represents SnO_x. Alloying of the metal oxide and noble metal phase can occur to form a distinct M₁M₂ alloy phase, resulting in an inverse bimetallic catalyst.

(Scheme 1, right). Accordingly, in-depth characterization and computational modeling of distinct surface sites are needed to develop a holistic view of these materials.

In this work, we examined IBCs supported on activated carbon for selective propionic acid (PA) hydrogenation to 1-

Received: June 28, 2019 Revised: October 24, 2019 Published: October 25, 2019

[†]National Bioenergy Center, National Renewable Energy Laboratory, Golden, Colorado 80401, United States

[‡]Davidson School of Chemical Engineering, Purdue University, West Lafayette, Indiana 47907, United States

[§]Chemical Sciences and Engineering Division, Argonne National Laboratory, Argonne, Illinois 60439, United States

propanol (1-PrOH). We identified the most promising catalyst to be RuSn with a Ru-to-Sn molar ratio of 1:1. We subsequently characterized the RuSn catalyst and performed density functional theory (DFT) calculations to elucidate its active species and catalytic mechanism. Phenylphosphonic acid (PPA) was cofed to inhibit Lewis acidic domains on Ru and RuSn, distinguishing catalytic roles in hydrogenation pathways. Extended X-ray absorption fine structure (EXAFS) spectroscopy of reduced catalysts was performed to obtain electronic and structural information. Mimicking EXAFS results, Ru(0001), Sn⁰/Ru(0001), and Sn₄O₄/Ru(0001) surfaces were constructed for DFT investigation, and the computed energetics enabled the interpretation of observed selectivity trends. As a result, we propose a reaction scheme consistent with DFT calculations, characterization, and observed reactivity that provides a basis for rational IBC design.

RESULTS

Catalyst Activity and Selectivity. Batch reactor catalyst screening identified that the RuSn catalyst, prepared as an IBC with Ru-to-Sn molar ratio of 1:1, is selective not only in succinic acid hydrogenation but also propionic acid hydrogenation, performing better than PdRe, PtSn, or their monometallic counterparts supported on powdered activated carbon (PAC) [see Figures S1-S3 of the Supporting Information (SI)]. While sparse literature is available on the aqueous-phase reduction of propionic acid, a comparison of RuSn to other catalysts for succinic acid reduction can be found in our previous work. The addition of Sn to Ru markedly reduced the formation of nonselective reduction and cracking products observed with monometallic Ru, indicative of over-reduction pathways to propane and cracking to form ethane and methane (Figure S2, SI). CO was not detected during the analysis of gas-phase reaction products, though it may be readily converted to CO2 via the water-gas shift reaction over Ru. 43,44

The high performance of RuSn-PAC led to the testing of RuSn supported on granular activated carbon (GAC) in a trickle bed flow reactor, as it is necessary to assess a more industrially relevant pellet-supported catalyst for stability at high conversions and high yield conditions. The results from the high-conversion time-on-stream run in this reactor are shown in Figure 1. At a WHSV (weight hourly space velocity) of 0.3 h⁻¹, RuSn-GAC demonstrated excellent selectivity for

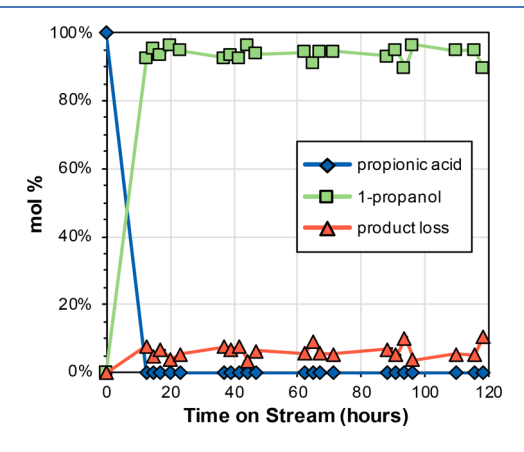


Figure 1. Propionic acid hydrogenation in a trickle bed flow reactor with RuSn-GAC. Conditions: 160 °C, 100 bar H₂ at 200 sccm, 1.0 g of RuSn-GAC, 25 g L⁻¹ propionic acid, WHSV 0.3 h⁻¹.

PA hydrogenation, achieving 1-PrOH yields of 94 \pm 2 mol % at 100% PA conversion while remaining stable for over 100 h on stream.

To discern RuSn-GAC reactivity, we measured PA hydrogenation rates and selectivities using low-conversion time-on-stream (<10%) experiments, with the results provided in Table 1. The rate of PA hydrogenation was 10 times higher

Table 1. Propionic Acid Hydrogenation Rates on Ru–GAC and RuSn–GAC Catalysts in a Flow Reactor at 160 $^{\circ}\text{C}$ and 100 bar H_2

		individi (% sele			
catalyst	overall rate, ^a mmol g ⁻¹ h ⁻¹	1- propanol ^b	lights ^c	H_2 uptake, d μ mol g^{-1}	
Ru-GAC	27.2 ± 0.2	2.6 (10)	24.6 (90)	47.5	
RuSn-GAC	2.6 ± 0.1	2.5 (95)	0.1 (5)	3.3	

"Measured from total PA consumption, conversion <10% b Measured via HPLC quantification. Calculated from the difference in the overall rate and 1-PrOH production rate. Determined from H_2 chemisorption on powder catalysts.

on Ru–GAC than on RuSn–GAC. Alongside rate changes, chemisorption experiments showed a 14-fold higher hydrogen uptake on Ru–PAC compared with RuSn–PAC, suggesting that Sn blocks H₂ adsorption and that the active sites involve Ru⁰. In addition, negligible CO uptake was previously observed on RuSn–PAC. While CO is known to poison Ru hydrogenation sites, ⁴⁵ the high activity observed over monometallic Ru would suggest that significant surface sites remain available and active for propionic acid reduction. However, product selectivities were vastly different, with PA mainly converted to light products (CO₂, methane, ethane, and propane) with Ru–GAC and to 1-PrOH with RuSn–GAC, implying that Sn influences the nature of the active site.

In unraveling the role of Sn, PPA was introduced to the mobile phase during PA hydrogenation over Ru–GAC and RuSn–GAC to target and inhibit surface metal oxide species. The change in PA hydrogenation rate upon PPA exposure is shown in Figure 2. Effectively, no change in the rate was observed on Ru–GAC, but an 80% reduction in the rate took place on RuSn–GAC. Interestingly, selectivity to 1-PrOH was maintained on RuSn–GAC during inhibition, implying that

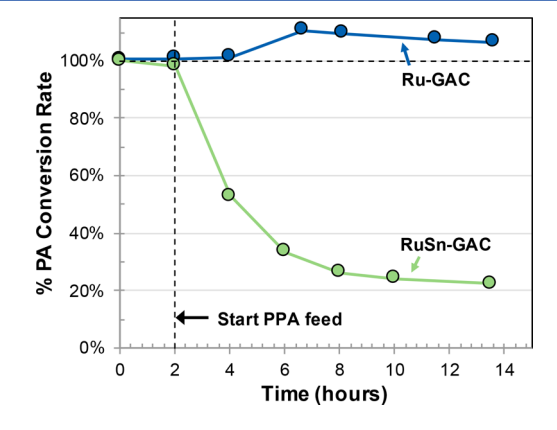


Figure 2. Change in the overall propionic acid conversion rate (listed in Table 1) as a function of time during exposure of the catalysts to a feed of 2 g^{-1} L⁻¹ PPA, 100 g^{-1} L⁻¹ propionic acid. Conditions: 160 °C, 200 sccm H₂, 100 bar H₂, propionic acid WHSV 4 h⁻¹.

the residual activity is not due to Ru⁰ sites but rather is related to the reversibility of deactivation (Figure S4,SI). Previous work demonstrated that PPA selectively binds to Lewis acidic oxides, 46-49 including self-assembled monolayers of phosphonic acids on SnO₂. 50,51 Additionally, these catalysts have been shown to exhibit weak Lewis acidic character, and X-ray photoelectron spectroscopy (XPS) demonstrated evidence of Sn oxide formation. Thus, the activity inhibition experiments suggest that oxidic Sn constitutes part of the RuSn IBC active site.

X-ray Absorption Spectroscopy. With a previous report pointing to oxide formation 1 and reactivity testing suggesting oxidic species to be active, further characterization was achieved by employing X-ray absorption spectroscopy (XAS) to probe the structure of RuSn IBC. Fresh and spent Ru-PAC and RuSn-PAC catalysts were examined under ambient and reducing conditions via controlled-atmosphere EXAFS at both Ru and Sn K-edges. X-ray absorption near-edge structure (XANES) and k^2 -weighted Fourier-transform spectra results, shown in Figure 3 and summarized in Table 2, reveal that the

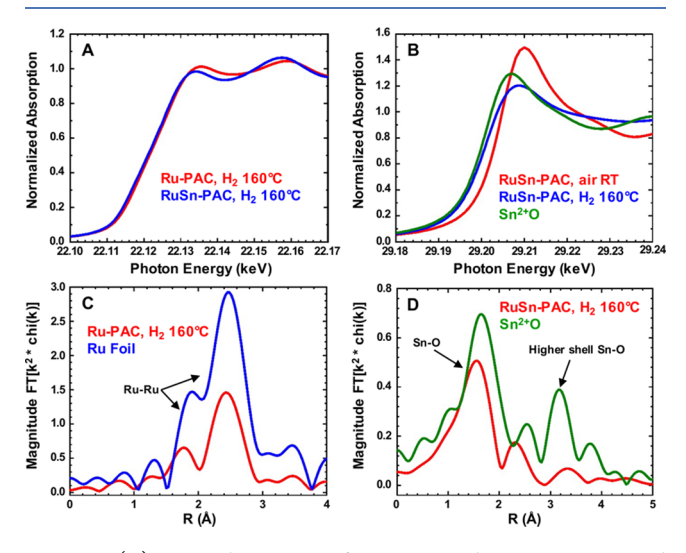


Figure 3. (A) Ru K-edge spectra of Ru–PAC and RuSn–PAC treated in H_2 at 160 °C, and (B) Sn K-edge spectra of fresh RuSn–PAC air-exposed and treated in H_2 at 160 °C compared to Sn²⁺O standard. (C) Ru k^2 -weighted Fourier-transformed spectra for Ru foil standard and Ru–PAC treated in H_2 at 160 °C. The low intensity of Ru–Ru scattering for reduced Ru–PAC, in contrast to the Ru foil, indicates small Ru nanoparticles, and (D) Sn k^2 -weighted Fourier-transformed spectra of RuSn–PAC treated in H_2 at 160 °C compared to Sn²⁺O standard.

spent, air-exposed catalysts contained oxidized metals Ru^{3+} and Sn^{4+} , while the fresh, air-exposed Ru–PAC contained some Ru^{0} . Treatment of all materials in $\mathrm{H_2}$ at 160 °C led to reduction of Ru^{3+} to Ru^{0} and Sn^{4+} to Sn^{2+} [see Table S1 and Figures S5 and S6 (SI) for more details].

The low-intensity of the Ru–Ru peak in the Ru EXAFS of Ru–PAC (Figure 3C) indicates that Ru formed small nanoparticles; this was true for fresh and spent Ru–PAC and RuSn–PAC catalysts, with particle sizes ranging from 2.5 to 4.5 nm, consistent with previous studies of these materials. There were no significant differences between fresh and spent catalysts, except for spent RuSn–PAC, which exhibited a smaller particle size upon treatment with H₂ at 160 °C. This suggests that the bimetallic catalyst rearranges under reaction-

like conditions. The Ru edge energy in the XANES region for RuSn-PAC (Figure 3A) was similar to that of Ru-PAC; however, the shape of the edge was shifted to slightly lower energy and the white line intensity was also slightly lower, similar but not identical to the spectra of a Ru₃Sn₇ standard (Figure S5, SI). This suggests that addition of Sn to Ru-PAC led to the formation of a nanoparticle partially comprised of a RuSn bimetallic phase. Direct evidence for this formation was difficult to observe by EXAFS analysis, since Ru and Sn have a similar number of electrons and scatter similarly. Further, near-surface alloy formation cannot be confirmed from this bulk particle analysis. The nearly identical edge energy of the Ru-PAC and RuSn-PAC catalysts suggests that most of the Ru was present as Ru nanoparticles, implying that the bimetallic RuSn phase may be present at the nanoparticle surface.

Sn K-edge spectra (Figure 3B) showed that, after treatment with $\rm H_2$ at 160 °C, most of the Sn in RuSn–PAC was reduced from Sn⁴⁺ to Sn²⁺, with an edge energy similar to that of Sn²⁺O. The k^2 -weighted Fourier-transform spectrum (Figure 3D) of RuSn–PAC after treatment with $\rm H_2$ at 160 °C showed fewer high-shell Sn–O–Sn peaks than bulk Sn²⁺O and Sn⁴⁺O₂, indicating that Sn²⁺O and Sn⁴⁺O₂ domains were quite small.

From the EXAFS results, we conclude that, at 160 °C under H₂, the Ru-PAC catalyst consisted of <5 nm Ru⁰. Under the same conditions, the RuSn-PAC catalyst surfaces consisted of <5 nm Ru⁰ nanoparticles with a surface that was enriched with Sn⁰, as well as small Sn²⁺O domains that were randomly dispersed on the surface (e.g., both on the activated carbon itself and on RuSn bimetallic nanoparticles). Observation of Sn oxide supports the above assertion that RuSn-GAC inhibition was due to PPA binding to Sn²⁺O sites. Previous characterization by chemisorption and temperature-programmed reduction showed negligible hydrogen and CO uptake with the same RuSn catalyst, in stark contrast to its monometallic Ru counterpart. XPS was also performed to confirm the presence of predominantly Ru⁰ with mixed Sn oxidation states (Sn⁰, Sn²⁺, Sn⁴⁺) on the reduced RuSn catalyst, which would support the presence of alloy Sn/Ru at the near-surface along with an oxide phase. Collectively, these results would suggest that the working RuSn catalyst is an inverse bimetallic. However, since the mechanism of the RuSn bimetallic active surface could not be deciphered from characterization and reaction testing alone, we then turned to DFT to provide further insight. On the basis of these characterization results, we constructed computational models to further probe reactivity by examining the main features of inverse bimetallic catalysts, namely, Sn⁰ in the alloyed phase and Sn²⁺O domains.

Modeling Inverse Bimetallics. We used periodic DFT calculations to examine surface—adsorbate interactions over representative models, chosen to emulate EXAFS results. We modeled Ru⁰ with Ru(0001),^{1,52,53} constructed near-surface Ru⁰Sn⁰ alloys by replacing surface Ru(0001) with Sn atoms,^{1,17,54,55} and optimized a small Sn₄O₄ cluster on Ru(0001) to represent Ru-supported Sn²⁺O domains (Table S2 and Figure S7, SI). The latter model was chosen to investigate the specific role of the Sn²⁺O domains in facilitating selective carboxylic acid hydrogenation, rather than study the effects on adjacent Ru sites. DFT-based equilibrium phase diagrams,^{56,57} addressing hydrogen adsorption and shown in Figure 4, revealed that Sn⁰ species inhibit Ru sites, resulting in lower coverage (see also Figure S8, SI). Hydrogen dissociation barriers also increased from 0 kJ mol⁻¹ on Ru(0001) to 11 and 15 kJ mol⁻¹ on 25% and 50% Sn/Ru(0001) (Figure S9, SI).

Table 2. EXAFS Results for Ru-PAC and RuSn-PAC Catalysts

			XANES energy, keV		Ru-O		Ru-Ru		Sn-O		oxidation state		
catalyst	condition	treatment	Ru	Sn	N	R, Å	N	R, Å	N	R, Å	Ru	Sn	estimated size, nm
Ru-PAC	fresh ^a	air, rt ^c	22.1264	nd^d	3.4	2	5.3	2.68	nd	nd	III	nd	nd
	fresh ^a	H ₂ , 160 °C	22.1181	nd	nd	nd	9.1	2.65	nd	nd	0	nd	4
	spent ^b	air, rt	22.1280	nd	5.8	2	nd	nd	nd	nd	III	nd	nd
	spent ^b	H ₂ , 160 °C	22.1171	nd	nd	nd	9.3	2.65	nd	nd	0	nd	4
RuSn-PAC	fresh ^a	air, rt	22.2128	29.2040	5.5	2	nd	nd	5.8	2.04	III	IV	nd
	fresh ^a	H ₂ , 160 °C	22.1171	29.0010	nd	nd	9.5	2.66	2.5	2.06	0	II	4.5
	spent ^b	air, rt	22.1285	29.2040	5.8	2	nd	nd	6	2.05	III	IV	nd
	spent ^b	H ₂ , 160 °C	22.1172	29.2000	nd	nd	7.1	2.65	1.9	2.05	0	II	2.5

"Unused, as-made catalyst. "Catalyst after 15 h of batch reaction, 100 bar of H₂, 160 °C, 25 g L⁻¹ propionic acid. "Room temperature. "Not detected.

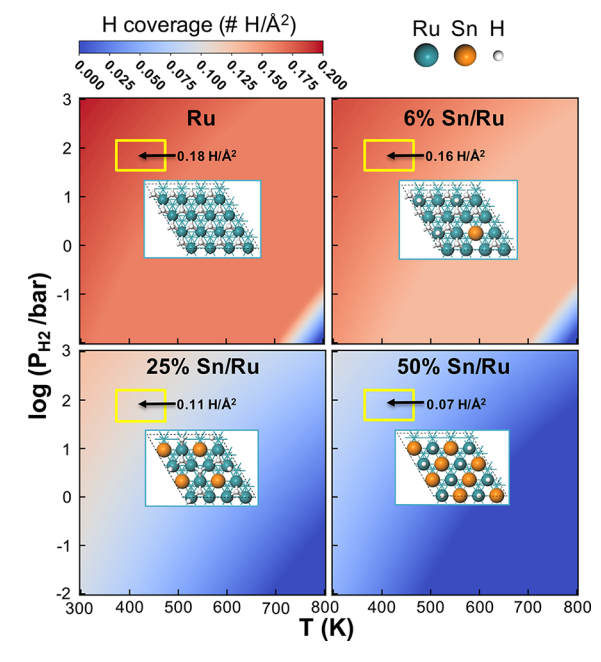


Figure 4. Phase diagrams showing hydrogen coverage on model surfaces as a function of temperature and pressure. Yellow rectangles represent the reaction conditions typical of propionic acid hydrogenation (i.e., $100-200\,^{\circ}\text{C}$ and $30-130\,\text{bar}\,\text{H}_2$). The insets show the equilibrium binding modes at these conditions, with the top layer represented with spheres.

Hydrogen is predicted to exhibit stronger affinity to SnO/Ru(0001), but the associated dissociation barrier was 99 kJ mol $^{-1}$, signifying kinetic limitations. Consistent with previous reports, we conclude that Ru sites are essential for $\rm H_2$ dissociation, while both $\rm Sn^0$ and oxidic $\rm Sn^{2+}$ species contribute to lower $\rm H_2$ uptake. 58 In the alloy models, we found that hydrogen interacts preferentially with Ru, suggesting that $\rm Sn^0$ solely isolates Ru sites without fundamentally altering their function. While site isolation was proposed for RhSn 59 and RuSn 35 catalysts and reflected in PtSn alloy computational studies, 54,55 this alone cannot explain the observed selectivity changes, which require a mechanistic understanding.

To gauge the role of Sn in RuSn IBCs, we evaluated PA reactivity on Ru(0001), 25% Sn/Ru(0001), and Sn₄O₄/Ru(0001) (Figure S7A,C,E, SI), referring to them hereafter as Ru, Sn/Ru, and SnO/Ru, respectively. On each model surface, we identified the likely mechanism by means of intrinsic energetics, i.e., surface-specific energies and barriers.

Reactions were deemed kinetically accessible on a given surface if the activation energy was below 110 kJ mol $^{-1}$, reflecting typical barriers that can be overcome under reaction conditions ($T=160~^{\circ}\mathrm{C}$ and $P_{\mathrm{H}_2}=100~\mathrm{bar}$). The results of this analysis in Figure 5 highlight the surfaces capable of promoting each reaction cycle, suggesting that both selective and nonselective reaction paths are accessible on metallic Ru and bimetallic Sn/Ru alloys while SnO/Ru is only capable of the desired, selective PA hydrogenation to 1-PrOH, consistent with our PPA inhibition experiments (see also Tables S10–S12 and Figures S16–S26, SI).

Desired Reduction to 1-PrOH. The desired reaction, PA hydrogenation to 1-PrOH, follows PA deoxygenation to propanal and its subsequent reduction to 1-PrOH. Analogous to acetic acid hydrogenation studies, ^{41,52,60} we considered three main paths to propanal: (i) direct C-OH scission to propionyl followed by C-H formation, (ii) C-H formation to propane-1-ol-1-olate followed by C-OH scission, and (iii) O-H scission to propionyl and C-H formation. Propanal reduction to 1-PrOH was found to be relatively facile on all model surfaces, irrespective of O-H or C-H formation first.

All three deoxygenation paths (Figure S16, SI) exhibited barriers lower than 88 kJ mol⁻¹ on Ru, in line with previous studies involving hydrogenation of acetic⁵² and propionic acids. 61 On Sn/Ru, only the propane-1-ol-1-olate deoxygenation path to propanal (reactions B1 and B2) was found to be kinetically accessible, while direct C-OH scission and C-O scission along the propionate path were 64 and 16 kJ mol⁻¹ more endothermic with substantially higher barriers. We did not attempt to discern the dominant paths beyond kinetic accessibility, since microkinetic modeling assumptions and extrinsic parameters can alter such conclusions. 52 Instead, we stress the existence of only one low-barrier path for PA deoxygenation on Sn/Ru, whereas multiple such paths likely contribute to the overall activity on Ru. The elevated deoxygenation barriers and fewer accessible paths leading to 1-PrOH on Sn/Ru suggest that alloying lowers IBC activity, as observed on RuSn-GAC.

In assessing SnO/Ru, we considered both the SnO cluster on its own and the reaction at the SnO-Ru interface. On SnO clusters, only the direct C-OH scission path to propanal was found to be kinetically accessible (reactions A1 and A2). Interestingly, the high-barrier C-H formation steps (reactions B1 and B3) were responsible for shutting down the propane-1-ol-1-olate deoxygenation path, which was accessible on both Ru and Sn/Ru. We attributed this and lower O-H formation

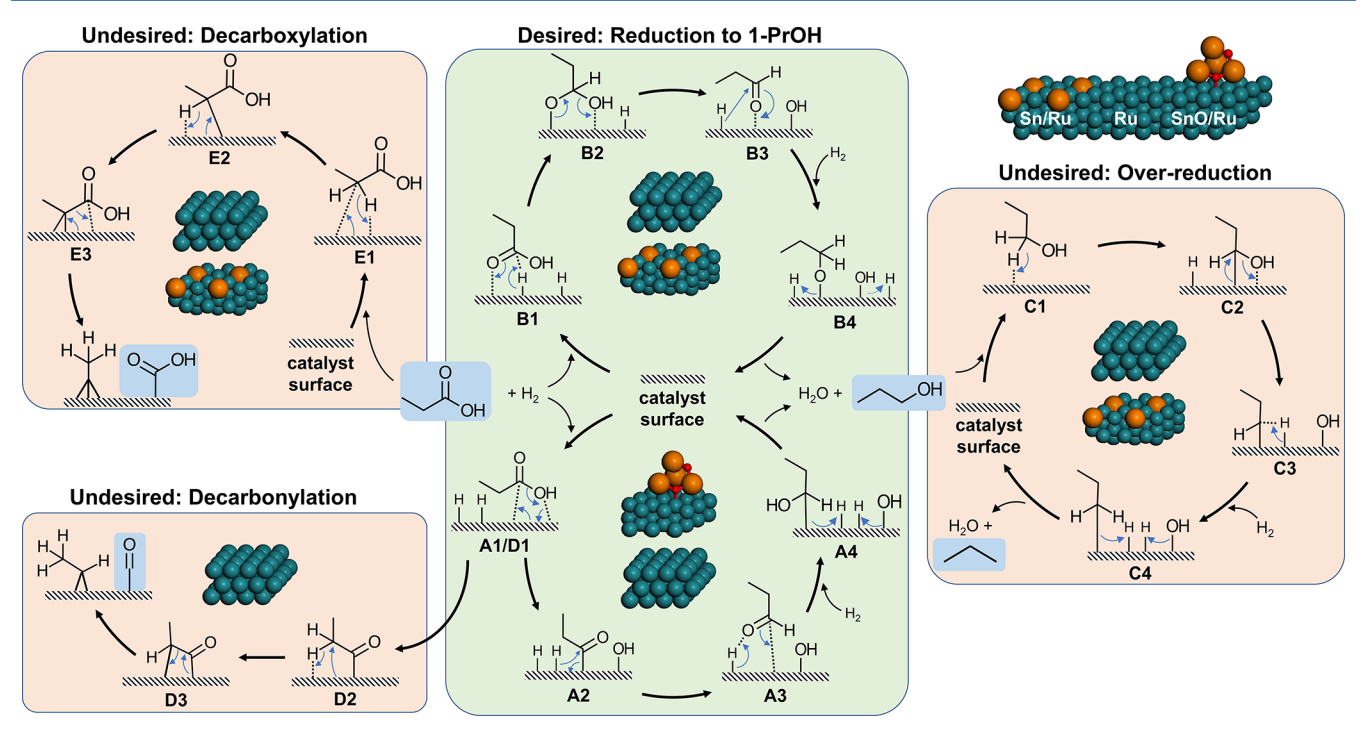


Figure 5. Overall mechanism for propionic acid hydrogenation to propanol via direct C–OH scission (pathway 1) and hydrogenation first (pathway 2), propanol overhydrogenation to propane (pathway 3), and initial steps in propanol decarbonylation (pathway 4) and decarboxylation (pathway 5). The inset images show catalytic functionalities with accessible barriers (below 110 kJ mol⁻¹) along each catalytic cycle.

barriers to the fundamental difference between metallic Ru and oxidic SnO/Ru, evidenced by significant shifts in Brønsted—Evans—Polanyi (BEP) relations in Figure 6. In fact, these distinctions may be responsible for synergistic effects between metallic Ru and oxidic SnO functionalities. In examining the SnO—Ru interface, we found that C—H formation can take place on Ru next to SnO (reaction B1), resulting in propane-1-ol-1-olate being adsorbed on SnO (Figure S21, SI). This intermediate can then undergo C—OH scission to propanal on SnO (reaction B2). The subsequent propanal hydrogenation also benefits from the dual functionality, showing facile O—H formation on SnO followed by C—H formation on Ru (reactions A3 and A4, Figure S22, SI). These results suggest that oxidic domains proximal to Ru can facilitate carboxylic acid hydrogenation to 1-PrOH as RuSn IBC active sites.

Assessing Selectivity. To better understand selectivity trends, we assessed 1-PrOH over-reduction to propane and initial steps leading to PA cracking via decarbonylation and decarboxylation (Table S10, SI). On Ru, all side reactions were found to be accessible. Propanol easily converts to propane starting with C-H scission [Figures 5C and S19 (SI)], consistent with results for ethanol decomposition.⁵³ Similarly, PA decarbonylation (Figure 5D) and decarboxylation [Figures 5E and S20 (SI) had barriers lower than 80 kJ mol⁻¹, aligning with Ru-GAC being nonselective. Sn⁰ incorporation into Ru resulted in higher C-OH, C-O, and C-H scission barriers, also observed on Sn-modified Pt and Ru surfaces for acetic acid hydrogenation. ^{17,24} We attributed this to the weaker binding of intermediates and related like-binding fragments, namely, CH₃, CH2, H, OH, and O (Table S13, SI). These surface species bind more weakly on Sn/Ru, causing the final states, which constitute C-Ru bonded fragments coadsorbed with H, OH, or O, to destabilize relative to the initial states. With destabilized final states, C-H and C-OH activation exhibit greater reaction energies and higher barriers consistent with

the BEP principle, leading to slower, yet still accessible, reactions on Sn/Ru.

In contrast to either Ru or Sn/Ru, no side reactions were energetically favored over SnO/Ru. On the basis of the BEP trend found in this work [Figures 6 and S13 (SI)], overreduction to propane was hindered by C-H scission/ formation (reactions C1 and C4), with barriers exceeding 120 kJ mol⁻¹ (Figure S19, SI). Similarly, C-H and C-C scission barriers along decarbonylation and decarboxylation exceeded 130 kJ mol⁻¹, suggesting that SnO/Ru is incapable of cracking. As with the above arguments, simple binding may explain this behavior. CO binds considerably more weakly on SnO/Ru compared with Ru or Sn/Ru (Table S13, SI), effectively destabilizing the final state in decarbonylation and increasing barriers associated with it. To summarize the computational findings, reflected in Figures 5 and S26 (SI), Ru is predicted to have low barriers along all paths, providing an explanation for its high activity but poor selectivity. Sn/Ru is predicted to exhibit barriers that are higher or comparable to those on Ru, supporting the notion that Sn⁰ inhibits and slows down reactions. The SnO/Ru model showed the greatest contrast between barriers along selective and nonselective paths, suggesting that this functionality is responsible for enhancing selectivity of RuSn IBCs.

DISCUSSION

Previous studies of bimetallic catalysts employed for selective hydrogenation of C=O moieties, be they carboxylic acids, esters, or aldehydes, have identified two possible active sites: (i) fully reduced M_1M_2 alloys of varying primary (M_1) and secondary (M_2) metal compositions $^{17,22-24,41,42}$ and (ii) $M_1M_2O_x$ involving an oxidized secondary component. $^{2,16,18,20,21,27-37}$ It is unsurprising that conclusions about the active site depend heavily on catalyst preparation and its resulting phases, 1,62 their characterization, 22,37 and theoretical

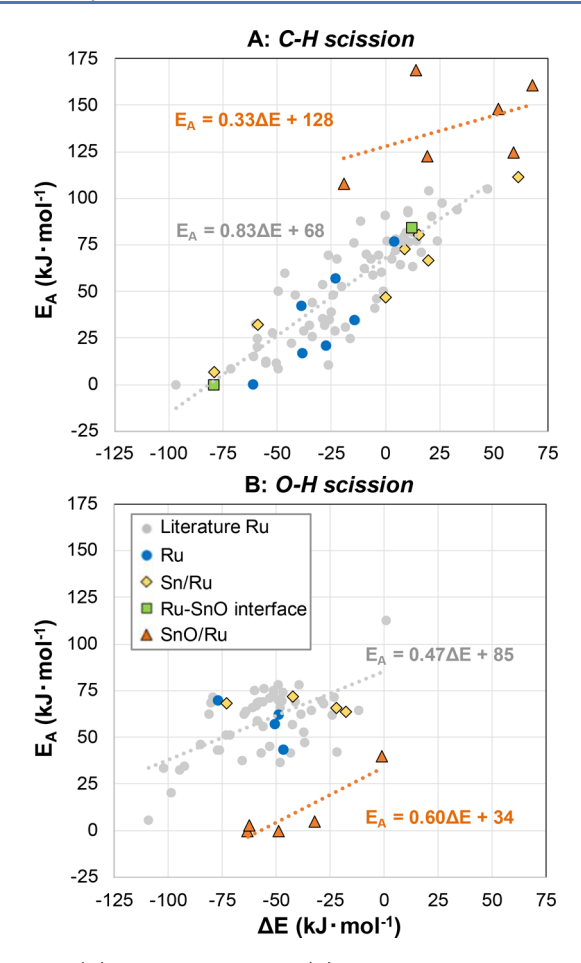


Figure 6. (A) C–H scission and (B) O–H scission BEP relations based on literature results for Ru(0001) (gray dots) and values obtained in this work for reactions at Ru(0001) (blue dots), 25% Sn/Ru(0001) (yellow diamonds), the interface of SnO cluster and Ru(0001) (green squares), and SnO/Ru(0001) (orange triangles). The results from this work are ZPE-corrected.

backing. 17,24,41 For instance, in the absence of information about the oxidation state of the catalyst, binary phase diagrams prompted the assertion that Ru₃Sn₇ alloys are responsible for selective hydrogenation of levulinic²² and butyric²³ acids. Similarly, XPS evidence for the alloying of Ru and Sn led Luo et al. to propose M₁M₂ active species for other carboxylic acids.24 Yet, there was no evidence discounting the participation of SnO_x species. 23,24 In fact, XPS of CoSn and RuSn catalysts revealed the presence of Sn²⁺ and Sn⁴⁺ species, suggesting that M₁M₂O_x may be responsible for improved selectivity in hydrogenation of fatty esters 32-34,63 and carboxylic acids. 1,24 For related PtSn catalysts, Alcala et al. identified PtSn alloy as the most abundant phase using Mössbauer spectroscopy and used DFT to show that Sn incorporation into Pt(111) increases barriers for ethanol dehydroxylation more so than for acetic acid dehydroxylation, suggesting M₁M₂ active species for selective acetic acid hydrogenation.¹⁷ Yet, the less abundant SnO_x was not assessed, despite being observed in the same samples, likely because of computational limitations. Meanwhile, single-crystal studies of PtSn(111) pointed to $M_1M_2O_x$ as the likely active species, stemming from observations that Sn⁰ incorporation lowers activity without altering selectivity in crotonaldehyde hydrogenation.36

In this work, we aimed to discern the structure-selectivity relationship by employing an IBC formulation associated with highly selective and process-relevant RuSn catalysts. We found that these catalysts exhibit high selectivity for PA to 1-PrOH and contain both M₁M₂ and M₁M₂O_x surfaces. The RuSn near-surface alloy, observed by EXAFS and modeled with DFT, energetically hinders hydrogenation to light products, largely shutting off the multiple pathways favored on monometallic Ru, yet still providing sites for H2 dissociation. Meanwhile, domains of SnO located near Ru⁰ were implicated as active sites by both PPA inhibition experiments and DFT, providing low-energy barriers to 1-PrOH formation while also shutting off undesired cracking pathways. Thus, both bimetallic arrangements are beneficial in constructing this highly selective IBC, a conclusion reached only through the integrated experimental and computational approach herein. Experimental evidence alone could not rule out either of the proposed bimetallic sites, while DFT relied on characterization to inform model surfaces. The resulting active site mechanism is consistent with models proposed previously, 33,34 wherein a fully reduced primary metal and an oxidized secondary metal work in concert. Our findings are also in line with the proposed Sn⁰ poisoning effect, 35,59 wherein Sn⁰ slows down the reactions, leading to undesired, cracking products. Similar trends were seen in DFT calculations for C–O, 17,24 C–C, 17 and C–H 54,55 scission on PtSn., and Ru₂Sn₇ surfaces.

On the basis of our findings, we can establish key design criteria for selective hydrogenation catalysts involving an interplay of M₁, M₁M₂, and M₁M₂O_r sites. An optimal catalyst for this type of reaction would consist of (1) a reduced metal capable of activating H_2 , (2) a secondary metal that can form a bimetallic phase to shut off nonselective hydrogenation pathways yet still be capable of H2 dissociation, and (3) a Lewis acid oxide vicinal to the reduced metal to facilitate selective hydrogenation. Optimizing IBCs to further increase the overall rate or reduce their cost will be crucial in the adoption of these catalysts. One possible approach involves computational screening of metallic and oxidic functionalities by utilizing a set of energetic descriptors, such as atomic binding energies coupled with BEP relations. Tailored synthesis and characterization strategies can then be employed to validate their composition and performance. In this work, the BEP relations developed for monometallic Ru could be readily applied to bimetallic alloys because of similarities in the binding of intermediates, hinting at the potential to reduce computational needs. Meanwhile, metal oxide clusters represent a significant shift from alloyed materials, suggesting that future catalyst formulations can be inspired by in silico tuning of C-H, O-H, and C-OH bond activations. Furthermore, these relations may apply beyond carboxylic acid chemistry. For instance, the increase in C-H formation barriers on Sn²⁺O domains supports the trends in selective crotonaldehyde hydrogenation over PtSn and RuSn, where SnO_x participation has been suggested. 36,37,42 While their applicability to other oxides remains to be explored, the implications for IBCs may be used more broadly to improve the carbon economy in CO2 reduction or natural gas processing, where the same elementary steps are involved.

It is important to note that this work focused on discerning the active sites for a single working catalyst with a specific Ru:Sn ratio of 1:1, which performed best for the aqueous-phase hydrogenation of succinic acid¹ and propionic acid.

SnO/Ru was found to be a dominant driver for this chemistry based on PPA inhibition experiments that demonstrate the need for surface Lewis acidity [Figures 2 and S4 (SI)] and DFT calculations that show the SnO/Ru has the greatest impact on selectivity. Still, alloy Sn/Ru may contribute to selective hydrogenation. Further efforts are needed to understand the influence of varying concentrations of alloy Sn/Ru and oxidic SnO/Ru sites that can result when varying the Ru:Sn ratio, synthesis conditions, and catalyst pretreatment procedures, which were beyond the scope of this work. As highlighted in this work, careful synthetic control with extensive material characterization and surface-specific catalytic performance measurements would be needed to elucidate the relative impact and codependency when varying the amount of surface exposed SnO/Ru and Sn/Ru alloy.

In considering future directions, extrinsic factors such as temperature, pressure, and condensed water can also affect catalyst surface coverage and hence the underlying energetics. For instance, microkinetic modeling has the potential to more precisely identify the contributions of each type of site, but it will require additional information about coverage effects on binding energies and intrinsic kinetics. Similarly, reaction conditions (operando) can provide structural information otherwise unavailable under reducing conditions (in situ). Accordingly, understanding how these dynamic effects impact computational and characterization results, as well as coupling the behavior to reaction kinetics, remains a worthy pursuit for screening and evaluating promising IBCs.

MATERIALS AND METHODS

Catalyst Synthesis. Catalyst synthesis details using a sequential metal deposition procedure have been described previously. Generally, primary metals were loaded onto the support at approximately 4 wt % and dried and reduced in H₂ for 4 h at 450 °C. Secondary metals were then loaded onto these materials at approximately 4 wt % and dried and reduced in H₂ for 4 h at 450 °C. Unless noted otherwise, the catalysts denoted as "metal"–PAC (e.g., Ru–PAC or RuSn–PAC) refer to catalysts on the powder support, whereas catalysts denoted as "metal"–GAC refer to catalysts on the granular support.

Propionic Acid Hydrogenation. Batch reactor catalyst screening experiments were performed in a Parr multibatch reactor system (Parr Instrument Co.). Powder catalyst and reaction solution (20 mL of 25 g $\rm L^{-1}$ aqueous propionic acid) were loaded into the reactors, which were sealed and purged with pressurized helium three times to remove ambient air. The reactors were then pressurized to 100 bar of $\rm H_2$ and heated to 160 °C. After 15 h at temperature, the reactors were quenched in a water bath and cooled to room temperature, and the solution was filtered and collected for product analysis.

Trickle bed flow reactor experiments were performed with the equipment and protocol described previously. The reactions were performed at 160 °C, 100 bar of H_2 , and 0.2 mL min⁻¹ liquid feed, at varying concentrations of aqueous PA. Reactor effluent was collected periodically for analysis. More detailed descriptions can be found in the SI.

Inhibition of catalysts with phenylphosphonic acid (PPA) was performed in the flow reactors, as described above. Once catalysts had reached steady state for propionic acid hydrogenation (fed at 0.2 mL min⁻¹, 100 g L⁻¹ propionic acid), the liquid feed bottle was changed to include PPA (fed at 0.2 mL

 \min^{-1} , 2 g L⁻¹ PPA, 100 g L⁻¹ propionic acid). Reactor effluent was collected periodically for analysis.

Liquid reaction products for both batch and flow experiments were analyzed with an Agilent 1100 series HPLC equipped with a Bio-Rad Aminex HPX-87H column and cation H guard column, operating at 85 °C, and a refractive index detector, with dilute sulfuric acid (0.01 N) as the mobile phase at 1.0 mL min⁻¹. Reactant and product concentrations were measured using authentic calibration standards prior to each use of the HPLC. The only compounds detected were propionic acid and 1-propanol; there were no peaks suggesting formation of any other condensed product (e.g., ethanol or 2-propanol).

EXAFS. X-ray absorption spectroscopy (XAS) experiments were performed at the Materials Research Collaborative Access Team (MRCAT) and CMC beamlines of the Advanced Photon Source at Argonne National Laboratory. Powder catalyst samples were loaded as self-supporting wafers in a sixsample stainless steel sample holder. For samples requiring pretreatment, the sample holder itself was loaded in a quartz sample tube equipped with gas and thermocouple ports and sealed at both ends by Kapton windows. The samples were heat-treated to 160 °C under flowing H₂ (4% H₂/He at 100 sccm) in a tube furnace for 30 min and then cooled under flowing He (100 sccm) to room temperature, sealed, and then placed in the beamline for XAS spectra collection. The XAS spectra were collected in transmission mode at the Ru (22.1172 keV) and Sn K-edges (29.2001 keV). The XAS data were fit using standard procedures based on WINXAS software, and k^2 -weighted Fourier-transform data were used to obtain the EXAFS coordination parameters with least-squares fits in q- and r-space of the isolated nearest neighbor.

Hydrogen Chemisorption. H_2 chemisorption of Ru–PAC and RuSn–PAC materials was performed on an Autochem II (Micrometrics) using a temperature-programmed desorption (TPD) method. Prior to analysis, samples were reduced under flowing H_2 (50 sccm, 10% H_2 in Ar) at 250 °C (2 °C min⁻¹) for 2 h and then cooled to 40 °C under inert flow. The materials were then heated to 450 °C (2 °C min⁻¹) and the desorbed H_2 was detected by TCD.

Computational Modeling. Periodic DFT calculations were used to analyze thermodynamics and intrinsic kinetics associated with propionic acid reactions on Ru(0001)-, Sn/Ru(0001)-, and Ru(0001)-supported Sn_4O_4 domains. For selective PA hydrogenation to 1-PrOH, transition states for each elementary step were computed explicitly using DFT. For nonselective routes, we used BEP relations for crude estimates, followed by DFT refinement. The details of our calculations are available in the Computational Modeling section of the SI.

ASSOCIATED CONTENT

Supporting Information

The Supporting Information is available free of charge on the ACS Publications website at DOI: 10.1021/acscatal.9b02726.

Text, figures, and tables concerning the catalyst synthesis method, catalyst batch reactor screening, gas-phase hydrogenation products, catalyst inhibition experiment, X-ray absorption spectroscopy, computational modeling, Brønsted–Evans–Polanyi relations, reaction mechanism, reaction energetics, and adsorption energetics (PDF)

AUTHOR INFORMATION

Corresponding Authors

*G.T.B. e-mail: gregg.beckham@nrel.gov. *D.R.V. e-mail: derek.vardon@nrel.gov.

ORCID

Jeffrey T. Miller: 0000-0002-6269-0620 Gregg T. Beckham: 0000-0002-3480-212X Derek R. Vardon: 0000-0002-0199-4524

Author Contributions

The following outlines the contributions of the researchers: conceptualization, V.V., T.R.E., G.T.B., D.R.V.; formal analysis, E.C.W., C.Y., J.T.M.; funding acquisition, G.T.B., D.R.V.; investigation, V.V., T.R.E., A.E.S., E.C.W., K.O.; supervision, J.T.M., G.T.B., D.R.V.; writing of the original draft, V.V., T.R.E.; review and editing the manuscript, V.V., T.R.E., G.T.B., D.R.V. Both V.V. and T.R.E. contributed equally to this work.

Notes

The authors declare the following competing financial interest(s): T.R.E., A.E.S., and D.R.V. are inventors on a patent application submitted by the Department of Energy on synthesis and use of bimetallic catalysts for selective carboxylic acid reduction (U.S. non-provisional patent application No. 15/828,658 filed on December 1, 2017).

ACKNOWLEDGMENTS

We thank the U.S. Department of Energy Bioenergy Technologies Office for funding this work as part of the Consortium for Computational Physics and Chemistry, Chemical Catalysis for Bioenergy Consortium, and Co-Optimization of Fuels & Engines (Co-Optima) through Contract No. DE-AC36-08GO28308 at the National Renewable Energy Laboratory. T.R.E. and G.T.B. thank the US Department of Energy Bioenergy Technologies Office for funding via grant number DE-FOA-0000996. E.C.W. and J.T.M. acknowledge financial support by the National Science Foundation under Cooperative Agreement No. EEC-1647722. Use of the Advanced Photon Source was supported by the U.S. Department of Energy, Office of Basic Energy Sciences, under contract no. DEAC02-06CH11357. MRCAT operations, beamline 10-BM, are supported by the Department of Energy and the MRCAT member institutions. The authors are grateful for supercomputer time on Stampede2 provided by the Texas Advanced Computing Center (TACC) under the National Science Foundation Extreme Science and Engineering Discovery Grant MCB-09159 to G.T.B. and the NREL Computational Science Center, which is supported by the DOE Office of Energy Efficiency and Renewable Energy under Contract no. DE-AC36-08GO28308.

REFERENCES

- (1) Vardon, D. R.; Settle, A. E.; Vorotnikov, V.; Menart, M. J.; Eaton, T. R.; Unocic, K. A.; Steirer, K. X.; Wood, K. N.; Cleveland, N. S.; Moyer, K. E.; Michener, W. E.; Beckham, G. T. Ru-Sn/AC for the Aqueous-Phase Reduction of Succinic Acid to 1,4-Butanediol under Continuous Process Conditions. ACS Catal. 2017, 7, 6207–6219.
- (2) Takeda, Y.; Shoji, T.; Watanabe, H.; Tamura, M.; Nakagawa, Y.; Okumura, K.; Tomishige, K. Selective Hydrogenation of Lactic Acid to 1,2-Propanediol over Highly Active Ruthenium—Molybdenum Oxide Catalysts. *ChemSusChem* **2015**, *8*, 1170—1178.
- (3) Gallezot, P. Conversion of Biomass to Selected Chemical Products. *Chem. Soc. Rev.* **2012**, *41*, 1538–1558.

- (4) Huber, G. W.; Corma, A. Synergies between Bio- and Oil Refineries for the Production of Fuels from Biomass. *Angew. Chem., Int. Ed.* **2007**, 46, 7184–7201.
- (5) Sauer, M.; Porro, D.; Mattanovich, D.; Branduardi, P. Microbial Production of Organic Acids: Expanding the Markets. *Trends Biotechnol.* **2008**, 26, 100–108.
- (6) Pleissner, D.; Dietz, D.; van Duuren, J. B. J. H.; Wittmann, C.; Yang, X.; Lin, C. S. K.; Venus, J. Biotechnological Production of Organic Acids from Renewable Resources. In *Biorefineries*; Advances in Biochemical Engineering/Biotechnology Vol. *166*; Springer: Cham, Switzerland, 2017; pp 373–410.
- (7) Chen, Y.; Nielsen, J. Biobased Organic Acids Production by Metabolically Engineered Microorganisms. *Curr. Opin. Biotechnol.* **2016**, *37*, 165–172.
- (8) Werpy, T.; Holladay, J.; White, J. Top Value Added Chemicals From Biomass: Volume I. Results of Screening for Potential Candidates from Sugars and Synthesis Gas; U.S. Department of Energy, Office of Scientific and Technical Information, 2004.
- (9) Farrell, J. Co-Optimization of Fuels & Engines (Co-Optima) Initiative: Recent Progress on Light-Duty Boosted Spark-Ignition Fuels/Engines; National Renewable Energy Lab. (NREL): Golden, CO, 2017.
- (10) Grasselli, R. K.; Trifirò, F. Acrylonitrile from Biomass: Still Far from Being a Sustainable Process. *Top. Catal.* **2016**, *59*, 1651–1658.
- (11) Karp, E. M.; Eaton, T. R.; Sàncĥez i Nogué, V.; Vorotnikov, V.; Biddy, M. J.; Tan, E. C. D.; Brandner, D. G.; Cywar, R. M.; Liu, R.; Manker, L. P.; Michener, W. E.; Gilhespy, M.; Skoufa, Z.; Watson, M. J.; Fruchey, O. S.; Vardon, D. R.; Gill, R. T.; Bratis, A. D.; Beckham, G. T. Renewable Acrylonitrile Production. *Science* **2017**, 358, 1307–1310.
- (12) Vardon, D. R.; Franden, M. A.; Johnson, C. W.; Karp, E. M.; Guarnieri, M. T.; Linger, J. G.; Salm, M. J.; Strathmann, T. J.; Beckham, G. T. Adipic Acid Production from Lignin. *Energy Environ. Sci.* **2015**, *8*, 617–628.
- (13) Vardon, D. R.; Rorrer, N. A.; Salvachua, D.; Settle, A. E.; Johnson, C. W.; Menart, M. J.; Cleveland, N. S.; Ciesielski, P. N.; Steirer, K. X.; Dorgan, J. R.; Beckham, G. T. cis,cis-Muconic Acid: Separation and Catalysis to Bio-Adipic Acid for Nylon-6,6 Polymerization. *Green Chem.* **2016**, *18*, 3397–3413.
- (14) Montazeri, M.; Zaimes, G. G.; Khanna, V.; Eckelman, M. J. Meta-Analysis of Life Cycle Energy and Greenhouse Gas Emissions for Priority Biobased Chemicals. *ACS Sustainable Chem. Eng.* **2016**, *4*, 6443–6454.
- (15) Corona, A.; Biddy, M. J.; Vardon, D. R.; Birkved, M.; Hauschild, M. Z.; Beckham, G. T. Life Cycle Assessment of Adipic Acid Production from Lignin. *Green Chem.* **2018**, *20*, 3857–3866.
- (16) Rachmady, W.; Vannice, M. A. Acetic Acid Reduction by H2 over Supported Pt Catalysts: A DRIFTS and TPD/TPR Study. *J. Catal.* **2002**, 207, 317–330.
- (17) Alcala, R.; Shabaker, J. W.; Huber, G. W.; Sanchez-Castillo, M. A.; Dumesic, J. A. Experimental and DFT Studies of the Conversion of Ethanol and Acetic Acid on PtSn-Based Catalysts. *J. Phys. Chem. B* **2005**, *109*, 2074–2085.
- (18) Primo, A.; Concepcion, P.; Corma, A. Synergy between the Metal Nanoparticles and the Support for the Hydrogenation of Functionalized Carboxylic Acids to Diols on Ru/TiO2. *Chem. Commun.* **2011**, *47*, 3613–3615.
- (19) Ly, B. K.; Minh, D. P.; Pinel, C.; Besson, M.; Tapin, B.; Epron, F.; Especel, C. Effect of Addition Mode of Re in Bimetallic Pd–Re/TiO2 Catalysts Upon the Selective Aqueous-Phase Hydrogenation of Succinic Acid to 1,4-Butanediol. *Top. Catal.* **2012**, *55*, 466–473.
- (20) Zhang, K.; Zhang, H.; Ma, H.; Ying, W.; Fang, D. Effect of Sn Addition in Gas Phase Hydrogenation of Acetic Acid on Alumina Supported PtSn Catalysts. *Catal. Lett.* **2014**, *144*, *691*–701.
- (21) Xu, G.; Zhang, J.; Wang, S.; Zhao, Y.; Ma, X. A Well Fabricated PtSn/SiO2 Catalyst with Enhanced Synergy between Pt and Sn for Acetic Acid Hydrogenation to Ethanol. *RSC Adv.* **2016**, *6*, 51005–51013.

(22) Wettstein, S. G.; Bond, J. Q.; Alonso, D. M.; Pham, H. N.; Datye, A. K.; Dumesic, J. A. RuSn Bimetallic Catalysts for Selective Hydrogenation of Levulinic Acid to γ -Valerolactone. *Appl. Catal., B* **2012**, *117*–118, 321–329.

- (23) Lee, J.-M.; Upare, P. P.; Chang, J.-S.; Hwang, Y. K.; Lee, J. H.; Hwang, D. W.; Hong, D.-Y.; Lee, S. H.; Jeong, M.-G.; Kim, Y. D.; Kwon, Y.-U. Direct Hydrogenation of Biomass-Derived Butyric Acid to n-Butanol over a Ruthenium—Tin Bimetallic Catalyst. *ChemSusChem* **2014**, *7*, 2998—3001.
- (24) Luo, Z.; Bing, Q.; Kong, J.; Liu, J.-y.; Zhao, C. Mechanism of Supported Ru3Sn7 Nanocluster-Catalyzed Selective Hydrogenation of Coconut Oil to Fatty Alcohols. *Catal. Sci. Technol.* **2018**, *8*, 1322–1332
- (25) Delhomme, C.; Weuster-Botz, D.; Kühn, F. E. Succinic Acid from Renewable Resources as a C4 Building-Block Chemical—a Review of the Catalytic Possibilities in Aqueous Media. *Green Chem.* **2009**, *11*, 13–26.
- (26) Pritchard, J.; Filonenko, G. A.; van Putten, R.; Hensen, E. J. M.; Pidko, E. A. Heterogeneous and Homogeneous Catalysis for the Hydrogenation of Carboxylic Acid Derivatives: History, Advances and Future Directions. *Chem. Soc. Rev.* **2015**, *44*, 3808–3833.
- (27) Mendes, M. J.; Santos, O. A. A.; Jordão, E.; Silva, A. M. Hydrogenation of Oleic Acid over Ruthenium Catalysts. *Appl. Catal., A* **2001**, *217*, 253–262.
- (28) Rachmady, W.; Vannice, M. A. Acetic Acid Hydrogenation over Supported Platinum Catalysts. *J. Catal.* **2000**, *192*, 322–334.
- (29) Chen, L.; Zhu, Y.; Zheng, H.; Zhang, C.; Zhang, B.; Li, Y. Aqueous-Phase Hydrodeoxygenation of Carboxylic Acids to Alcohols or Alkanes over Supported Ru Catalysts. *J. Mol. Catal. A: Chem.* **2011**, 351, 217–227.
- (30) Chen, L.; Zhu, Y.; Zheng, H.; Zhang, C.; Li, Y. Aqueous-Phase Hydrodeoxygenation of Propanoic Acid over the Ru/ZrO2 and Ru–Mo/ZrO2 Catalysts. *Appl. Catal., A* **2012**, *411–412*, 95–104.
- (31) Chen, L.; Li, Y.; Zhang, X.; Zhang, Q.; Wang, T.; Ma, L. Mechanistic Insights into the Effects of Support on the Reaction Pathway for Aqueous-Phase Hydrogenation of Carboxylic Acid over the Supported Ru Catalysts. *Appl. Catal.*, A 2014, 478, 117–128.
- (32) Deshpande, V. M.; Ramnarayan, K.; Narasimhan, C. S. Studies on Ruthenium-Tin Boride Catalysts II. Hydrogenation of Fatty Acid Esters to Fatty Alcohols. *J. Catal.* **1990**, *121*, 174–182.
- (33) Pouilloux, Y.; Autin, F.; Guimon, C.; Barrault, J. Hydrogenation of Fatty Esters over Ruthenium—Tin Catalysts; Characterization and Identification of Active Centers. *J. Catal.* **1998**, *176*, 215–224.
- (34) Pouilloux, Y.; Piccirilli, A.; Barrault, J. Selective Hydrogenation into Oleyl Alcohol of Methyl Oleate in the Presence of RuSnAl2O3 Catalysts. J. Mol. Catal. A: Chem. 1996, 108, 161–166.
- (35) Coq, B.; Kumbhar, P. S.; Moreau, C.; Moreau, P.; Figueras, F. Zirconia-Supported Monometallic Ru and Bimetallic Ru-Sn, Ru-Fe Catalysts: Role of Metal Support Interaction in the Hydrogenation of Cinnamaldehyde. *J. Phys. Chem.* **1994**, *98*, 10180–10188.
- (36) Jerdev, D. I.; Olivas, A.; Koel, B. E. Hydrogenation of Crotonaldehyde over Sn/Pt(111) Alloy Model Catalysts. *J. Catal.* **2002**, 205, 278–288.
- (37) Kennedy, G.; Melaet, G.; Han, H.-L.; Ralston, W. T.; Somorjai, G. A. In Situ Spectroscopic Investigation into the Active Sites for Crotonaldehyde Hydrogenation at the Pt Nanoparticle—Co3O4 Interface. ACS Catal. 2016, 6, 7140—7147.
- (38) Graciani, J.; Mudiyanselage, K.; Xu, F.; Baber, A. E.; Evans, J.; Senanayake, S. D.; Stacchiola, D. J.; Liu, P.; Hrbek, J.; Sanz, J. F.; Rodriguez, J. A. Highly Active Copper-Ceria and Copper-Ceria-Titania Catalysts for Methanol Synthesis from CO2. *Science* **2014**, 345, 546–550.
- (39) Kattel, S.; Ramírez, P. J.; Chen, J. G.; Rodriguez, J. A.; Liu, P. Active Sites for CO2 Hydrogenation to Methanol on Cu/ZnO Catalysts. *Science* **2017**, 355, 1296–1299.
- (40) Rodríguez, J. A.; Hrbek, J. Inverse Oxide/Metal Catalysts: A Versatile Approach for Activity Tests and Mechanistic Studies. *Surf. Sci.* **2010**, *604*, 241–244.

(41) Pallassana, V.; Neurock, M. Reaction Paths in the Hydrogenolysis of Acetic Acid to Ethanol over Pd(111), Re(0001), and PdRe Alloys. *J. Catal.* **2002**, 209, 289–305.

- (42) Riguetto, B. A.; Rodrigues, C. E. C.; Morales, M. A.; Baggio-Saitovitch, E.; Gengembre, L.; Payen, E.; Marques, C. M. P.; Bueno, J. M. C. Ru-Sn Catalysts for Selective Hydrogenation of Crotonaldehyde: Effect of the Sn/(Ru+Sn) Ratio. *Appl. Catal., A* **2007**, *318*, 70–78.
- (43) Liu, B.; Huang, T.; Zhang, Z.; Wang, Z.; Zhang, Y.; Li, J. The Effect of the Alkali Additive on the Highly Active Ru/C Catalyst for Water Gas Shift Reaction. *Catal. Sci. Technol.* **2014**, *4*, 1286–1292.
- (44) Venugopal, A.; Scurrell, M. S. Hydroxyapatite as a Novel Support for Gold and Ruthenium Catalysts: Behaviour in the Water Gas Shift Reaction. *Appl. Catal., A* **2003**, *245*, 137–147.
- (45) Okuhara, T.; Kimura, T.; Kobayashi, K.; Misono, M.; Yoneda, Y. Effects of Dispersion in Carbon Monoxide Adsorption and Carbon Monoxide Hydrogenation over Alumina-supported Ruthenium Catalysts. *Bull. Chem. Soc. Jpn.* **1984**, *57*, 938–943.
- (46) Gao, W.; Dickinson, L.; Grozinger, C.; Morin, F. G.; Reven, L. Self-Assembled Monolayers of Alkylphosphonic Acids on Metal Oxides. *Langmuir* **1996**, *12*, 6429–6435.
- (47) Mutin, P. H.; Lafond, V.; Popa, A. F.; Granier, M.; Markey, L.; Dereux, A. Selective Surface Modification of SiO2–TiO2 Supports with Phosphonic Acids. *Chem. Mater.* **2004**, *16*, 5670–5675.
- (48) Eaton, T. R.; Boston, A. M.; Thompson, A. B.; Gray, K. A.; Notestein, J. M. Counting Active Sites on Titanium Oxide—Silica Catalysts for Hydrogen Peroxide Activation through In Situ Poisoning with Phenylphosphonic Acid. *ChemCatChem* **2014**, *6*, 3215–3222.
- (49) Thornburg, N. E.; Nauert, S. L.; Thompson, A. B.; Notestein, J. M. Synthesis—Structure—Function Relationships of Silica-Supported Niobium(V) Catalysts for Alkene Epoxidation with H2O2. *ACS Catal.* **2016**, *6*, 6124–6134.
- (50) Holland, G. P.; Sharma, R.; Agola, J. O.; Amin, S.; Solomon, V. C.; Singh, P.; Buttry, D. A.; Yarger, J. L. NMR Characterization of Phosphonic Acid Capped SnO2 Nanoparticles. *Chem. Mater.* **2007**, 19, 2519–2526.
- (51) Serre, C.; Auroux, A.; Gervasini, A.; Hervieu, M.; Férey, G. Hexagonal and Cubic Thermally Stable Mesoporous Tin(IV) Phosphates with Acidic and Catalytic Properties. *Angew. Chem., Int. Ed.* **2002**, *41*, 1594–1597.
- (52) Olcay, H.; Xu, Y.; Huber, G. W. Effects of Hydrogen and Water on the Activity and Selectivity of Acetic Acid Hydrogenation on Ruthenium. *Green Chem.* **2014**, *16*, 911–924.
- (53) Chiu, C.-c.; Genest, A.; Rösch, N. Decomposition of Ethanol Over Ru(0001): A DFT Study. *Top. Catal.* **2013**, *56*, 874–884.
- (54) Yang, M.-L.; Zhu, Y.-A.; Zhou, X.-G.; Sui, Z.-J.; Chen, D. First-Principles Calculations of Propane Dehydrogenation over PtSn Catalysts. *ACS Catal.* **2012**, *2*, 1247–1258.
- (55) Hook, A.; Massa, J. D.; Celik, F. E. Effect of Tin Coverage on Selectivity for Ethane Dehydrogenation over Platinum—Tin Alloys. *J. Phys. Chem. C* **2016**, *120*, 27307—27318.
- (56) Rogal, J.; Reuter, K.; Scheffler, M. Thermodynamic Stability of PdO Surfaces. *Phys. Rev. B: Condens. Matter Mater. Phys.* **2004**, *69*, 075421.
- (57) Ferguson, G. A.; Vorotnikov, V.; Wunder, N.; Clark, J.; Gruchalla, K.; Bartholomew, T.; Robichaud, D. J.; Beckham, G. T. Ab Initio Surface Phase Diagrams for Coadsorption of Aromatics and Hydrogen on the Pt(111) Surface. *J. Phys. Chem. C* **2016**, *120*, 26249–26258.
- (58) Wijzenbroek, M.; Kroes, G. J. The Effect of the Exchange-Correlation Functional on H2 Dissociation on Ru(0001). *J. Chem. Phys.* **2014**, *140*, 084702.
- (59) Ferretti, O. A.; Bournonville, J. P.; Mabilon, G.; Martino, G.; Candy, J. P.; Basset, J. M. Surface Organometallic Chemistry on Metals: Part IV. Selective Hydrogenation of Ethyl Acetate to Ethanol on RhSn/SiO2 Bimetallic Catalysts: A Mechanistic Study. *J. Mol. Catal.* 1991, 67, 283–294.

(60) Olcay, H.; Xu, L.; Xu, Y.; Huber, G. W. Aqueous-Phase Hydrogenation of Acetic Acid over Transition Metal Catalysts. *ChemCatChem* **2010**, *2*, 1420–1424.

- (61) Lu, J.; Faheem, M.; Behtash, S.; Heyden, A. Theoretical Investigation of the Decarboxylation and Decarbonylation Mechanism of Propanoic Acid over a Ru(0001) Model Surface. *J. Catal.* **2015**, 324, 14–24.
- (62) Coloma, F.; Sepúlveda-Escribano, A.; Fierro, J. L. G.; Rodríguez-Reinoso, F. Crotonaldehyde Hydrogenation over Bimetallic PtSn Catalysts Supported on Pregraphitized Carbon Black. Effect of the Preparation Method. *Appl. Catal., A* **1996**, *148*, 63–80.
- (63) Pouilloux, Y.; Autin, F.; Barrault, J. Selective Hydrogenation of Methyl Oleate into Unsaturated Alcohols: Relationships between Catalytic Properties and Composition of Cobalt—Tin Catalysts. *Catal. Today* **2000**, *63*, 87–100.
- (64) Wang, S.; Vorotnikov, V.; Vlachos, D. G. Coverage-Induced Conformational Effects on Activity and Selectivity: Hydrogenation and Decarbonylation of Furfural on Pd(111). ACS Catal. 2015, S, 104–112.
- (65) Zhao, Z.-J.; Chiu, C.-c.; Gong, J. Molecular Understandings on the Activation of Light Hydrocarbons over Heterogeneous Catalysts. *Chem. Sci.* **2015**, *6*, 4403–4425.